Microwave Limb Sounder THz Module on Aura

Herbert M. Pickett, *Member, IEEE*

***Abstract*—The objective of the Microwave Limb Sounder THz module on the Aura satellite is to measure stratospheric and mesospheric OH. This paper describes the optical design, alignment, calibration, and performance of the THz module. The calibration uncertainty for one limb scan is substantially less than the precision due to radiometric noise. For averages of many scans, the dominant calibration uncertainty of 2% is due to uncertainty in beam efficiency.**

***Index Terms*—Mesosphere, OH, stratosphere, THz.**

I. INTRODUCTION

THE Microwave Limb Sounder (MLS) THz module on the Aura satellite was developed to measure the OH radical in the stratosphere and mesosphere using heterodyne detection of thermal emission. The OH emission comes from rotational fine structure lines near 2.5 THz (119 μm). The OH lines indicated in Table I are each split into three hyperfine components [1]. The frequency given is for the strongest component. In addition, pointing information is obtained from O_2 emission from a nearby magnetic-dipole transition. Table I also shows the strongest O_3 lines seen within the instrument passband.

The limb emission is detected with heterodyne radiometry using a methanol gas laser local oscillator (GLLO) and waveguide diode mixers [2]. Table I also gives the oscillation frequency of the GLLO, which is stable to ±1 MHz. To improve sensitivity, both polarizations of the OH lines are detected independently. After mixing, each band is further down-converted with a second local oscillator and detected in a 25-channel filterbank. Except for special check-out operations, band 20 is not normally connected to a filterbank. Bands 15–17 share the same mixer and receive linearly polarized radiation along a horizontal axis when the boresight is horizontal (perpendicular to the spacecraft nadir direction). Bands 18–20 also share a mixer and receive the orthogonal linear polarization. When observing the limb, the boresight is approximately 25° below the local horizontal and the polarization axes are rotated by a corresponding amount.

The MLS instrument package on the Aura spacecraft is divided into the THz, GHz, and spectrometer modules. An overview of the MLS instrument is given in Waters *et al.* [3].

In the discussions to follow, minor frame (MIF) is the time interval (nominally 0.167 s) for signal integration. A science data frame is generated each MIF. An MAF is the repeat interval for a limb angle scan and calibration views and is nominally 148 MIFs (24.667 s). There are 240 MAFs per orbit. The duration of a MIF is chosen so that the duration of 148 × 240 MIFs is slightly less than the orbital period. The difference is made up just after the Aura descending equator crossing with MAFs that are 149 MIFs in duration. These adjustments assure that the limb scans are performed at the same latitude each orbit. Both GHz and THz module limb scans begin at the same time, but the actual scan profile is different for the two modules.

TABLE I
MLS THz MODULE MOLECULE AND GLLO FREQUENCIES

Band	Molecule	Frequency / GHz
15, 18	OH	2514.317
16, 19	OH	2509.949
16, 19	O_3	2509.560
17, 20	O_2	2502.324
17, 20	O_3	2543.208
	GLLO	2522.782

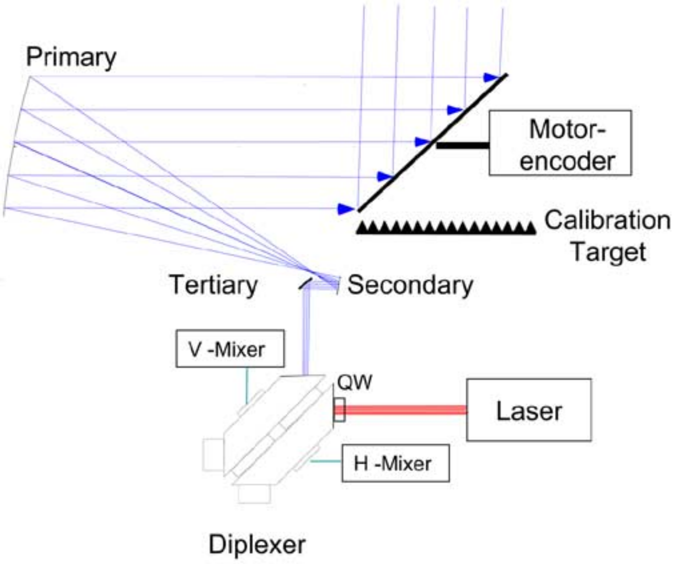

Fig. 1. MLS THz module optical schematic.

II. ALIGNMENT

Fig. 1 shows the optical design schematic of the MLS THz module. The first mirror, attached to a motor-encoder, is the flat scan mirror. It has a $\sqrt{2}:1$ elliptical outline with a 267-mm small dimension. Mirror scan angle is measured with a 23-b optical encoder that is embedded in the feedback control loop of the motor.

The telescope is an off-axis Gregorian design manufactured from aluminum with uncoated diamond-turned surfaces. The primary is a 600-mm focal length 228-mm diameter parabola. The primary is the limiting pupil diameter in the optical system and is illuminated with a Gaussian beam at the −30-dB power contour. The secondary is a 20-mm diameter off-axis ellipse, and the tertiary is flat. An important feature of the telescope

Manuscript received April 25, 2005; revised September 15, 2005. This work was performed at the Jet Propulsion Laboratory, California Institute of Technology, under contract with the National Aeronautics and Space Administration.

The author is with the Jet Propulsion Laboratory, California Institute of Technology, Pasadena, CA 91109 USA (e-mail: herbert.m.pickett@jpl.nasa.gov).

Digital Object Identifier 10.1109/TGRS.2005.862667

is that there is a 1.6-mm aperture at the focus of the primary that aids in alignment and functions as a light baffle. The telescope assembly was interferometrically tested at the manufacturer using a 3-μm laser, with the focal-plane aperture as a reference datum, and indicated a surface root mean square (rms) accuracy of better than 1 μm. This surface accuracy is substantially better than needed for THz performance, but is needed to make interferometric testing possible.

The atmospheric and GLLO signals are combined with a diplexer shown in Fig. 1. The diplexer is a 4-port polarizing Michelson (or Martin–Puplett) interferometer that contains two free-standing polarizing grids [2]. The GLLO is linearly polarized at 45° and the signal is unpolarized. The first grid spatially combines the signal and GLLO beams, but splits the power of the signal and GLLO beams into orthogonal polarizations. The second grid is the interferometer beam splitter and works with roof-top reflectors to align the polarizations of the signal and GLLO beams, as required by the mixers. Since MLS has intermediate (IF) frequencies that span a large frequency range, there is no tuning position that is simultaneously optimum for all IF frequencies. The choice used here de-tunes the diplexer for the GLLO wavelength to 80% transmission and allows better side-band rejection for the OH signals (see below).

The mixer assemblies both have elliptical feed mirrors to focus the incoming light on the mixer and its integrated horn. For alignment, the elliptical mirror can be replaced with a flat mirror that has the same chief ray as the long focus of the elliptical mirror. In this way, the mixer can be optically placed at the short focus of the ellipse. The angular position and focal depth of the mixer are not particularly sensitive, but the transverse position of the mixer is very sensitive. The apparent mixer position is adjusted by shimming the mount points on the feed mirror.

The strategy for system alignment uses white-light autocollimators and reference reticles for all critical tests. Alignment is difficult with visible lasers because the diamond-turned surfaces tend to diffract the laser beam. Direct alignment using THz sources is not practical both because the precision that can be obtained is poor and because the absorption length due to humidity is approximately 1 m.

The first step in instrument alignment is to align the diplexer with the telescope. For this purpose, a reflecting reticle is placed at the telescope input to the diplexer. An autocollimator is positioned to be centered in the telescope main aperture and to have an infinite focus that is centered on the focal aperture. Both the position and angle of the diplexer are then adjusted to bring the reticle onto the axis of the autocollimator.

Alignment of the laser with the diplexer was obtained with a transfer template located on the THz module structure straddling the GLLO optics path. First, the template was centered and rotated so that a reticle on the template had a common centerline and a parallel surface normal with a reticle located on the GLLLO input to the diplexer. Then this template was taken to the laser manufacturer and the laser was aligned to the template. Thermal imaging of GLLO power at the GLLO entrance of the diplexer showed that no further alignment was needed after delivery to instrument integration.

Within a month of instrument delivery, a significant standing wave between the laser output coupler and the mixers was discovered during spectral calibration. The frequency dependence of the standing wave implied a length that showed that the standing wave was likely due to a path that included the mixer and the output coupler of the laser. Some of the signal with the wrong polarization reflects off the mixer and is transmitted back through the diplexer and routed toward the laser. Since the laser is a good reflector at signal frequencies, this signal reflects back toward the mixer (thereby forming the standing wave). Fortunately, the problem was greatly reduced by inserting a quartz 1/4 wave plate in the GLLO beam using the attach points for the alignment reticle on the diplexer (see location marked **QW** in Fig. 1). The 1/4 wave plate has 75% transmission and is placed in the beam with its optical axis at 45°. Since the laser polarization is nominally at 45°, the plate attenuates but does not change the polarization state of the laser. However, for the vertically or horizontally polarized mixer return, the wave plate converts the unwanted signal to the orthogonal polarization and returns it to the other mixer.

III. FIELD-OF-VIEW CALIBRATION

The approach to measurement of the vertical field of view (FOV) is to use a compact range that is scanned in the vertical only. Measurements are made in vacuum to avoid water-vapor attenuation and concomitant loss in sensitivity. The compact range consists of a test parabola and a medium pressure mercury arc in a elliptical cavity. This mercury arc is a replacement far infrared source in a Bruker 120 interferometer. It is housed in a quartz envelope with 1-cm diameter and 5-cm length. The arc centerline is at one focus of the elliptical cavity and a slit aperture is at the other focus. This aperture is at the focus of a 600-mm focal length 267-mm diameter off-axis parabola that was machined at the same time as the MLS THz primary. This mirror contains an alignment flat that is perpendicular to the optical axis of the parabola. The surface figure of the mirror was interferometrically tested at 3-μm wavelength using the alignment flat as a reference. During alignment of the test parabola, an autocollimator is positioned perpendicular to the alignment flat, and then the slit is positioned in the field of the autocollimator. The faces of the slit in the direction of the test parabola are wedged at 15° over an angular extent of $\pm 1.5°$ to reduce standing waves with the instrument. The slit used for the FOV calibration is 0.216 mm wide. In effect, the slit source and parabola appear to be a synthetic atmosphere with a very hot layer in comparison with the surroundings. The one-dimensional integrated field of view is then determined directly by scanning the instrument using the flight scan mechanism. These patterns are absolute, because the FOV scans are referenced by imaging the visible light from the mercury source onto the focal aperture of the MLS THz primary. The focal aperture is then referenced through alignment cubes to the spacecraft.

The horizontal FOV is less critical than the vertical so it was not measured directly. The horizontal FOV can be inferred by two lines of reasoning. First, the MLS optics have a limiting 1.6-mm aperture at the primary focus that limits the possible deviations of the horizontal boresight to $\pm 0.075°$. Second, the optical system is designed to have a circular beam cross section which means that the horizontally polarized channel should have a horizontal pattern which matches the vertical pattern of the vertically polarized channel. A reciprocal inference can be made about the horizontal pattern of the vertically polarized channel.

Boresight is measured in much the same way as the vertical FOV, except that the measurements are made in air over the central part of the pattern. The THz boresight is referenced to a visible image of the source slit projected onto the instrument primary focus aperture. This image is observed with a closed-circuit TV so that the instrument platform is not distorted by human observers, as well as to protect users from the intense visible and UV light from the mercury arc source. In a separate measurement, the horizontal and vertical positions of the aperture are referenced to the spacecraft mounting points of the THz module using three theodolites.

A. Prelaunch Pointing Measurements

The FOV is continuously scanned in three 1° segments at a rate of 0.01° per MIF. These segments overlap by 0.1° and are combined together and truncated at the edges to produce a ±1.3° FOV pattern. The maximum angular extent is set by the angular extent of the wedged slit assembly at the focus of the test parabola. The effect of the 0.216-mm slit (0.0206° angular size) is to convolve the true FOV with a rectangular filter. The effect of the continuous scan is to convolve the FOV with a second smaller rectangular filter. The true FOV can be obtained by deconvolving the effects of the finite slit width and the continuous scan. Equivalently, the true FOV can be obtained numerically by Fourier transforming the measured pattern, by dividing the resulting aperture autocorrelation function by the two sinc functions out to the telescope diameter (and setting larger distances to zero), and then by back transforming the corrected autocorrelation function to the angular domain. Because of edge taper, the autocorrelation function may decrease rapidly as a function of radius, but the maximum limit is given by the telescope diameter. The size of the slit is chosen such that the Fourier transform of its angular extent produces a sinc function that has a value of 0.45 at a distance equal to the diameter of the MLS THz parabola. The signal integration and sample spacing is chosen so that the Fourier transform of the box-car integration produces a sinc function that has a value of 0.82 at a distance equal to the diameter of the MLS THz parabola. The noise amplification of the deconvolution is partially offset by the oversampling of the FOV relative to the slit size.

For FOV measurements, we combine filterbank channels for an effective bandwidth of 1300 MHz. Unfortunately, the nature of the source means that the measurements will be a weighted average of upper and lower side-band patterns. Any trend with frequency will be masked by the necessity of averaging the upper and lower side-band FOV patterns. However, second-order trends can be observed as well as differences in sidelobe levels that are dependent on IF. The small ratio of IF frequency to input sky frequency (0.008) implies that there should be little dependence of FOV on sky frequency.

Given that radiometric noise for the full 1300-MHz bandwidth is likely to be dominated by drift effects, we estimate $\Delta T_{\mathrm{rms}} = 4$ K (DSB) for 0.167 s of integration and 1300 MHz bandwidth. For the 0.216-mm slit, limb-equivalent angular width is 1.1 km and the boresight radiance contrast is 900 K. We made 1 h of measurements (146 scans) for each scan segment for a total of 3 h of measuring time. The estimated rms noise level is -36 dB.

The accuracy of the FOV patterns is actually limited by the need to establish a zero-power offset. The measured patterns were differenced with a view of the ambient calibration load, but the wedged reflecting surfaces near the slit reflect a slightly different temperature than that of the ambient target. A first estimate of the zero-power offset is to average the pattern outside the main lobe. This estimate is refined by noting that an inappropriate offset appears in the aperture autocorrelation function as a narrow sinc near zero displacement. The offset can be refined by making the autocorrelation function smooth near zero displacement. The estimated uncertainty of this offset is -24 dB.

A second effect that must be recognized is that the standing waves of the test system with the THz instrument are different at the center of the pattern when the radiation from the instrument enters the source compared with other angles where the radiation is reflected off of the wedged slit assembly. This effect shows up in the pattern as a notch at the exact center of the pattern and shows up in the corrected autocorrelation function as a constant offset. We correct the measured and sinc-corrected correlation function by an offset that makes the correlation function zero at a displacement equal to the diameter of the primary. The effect in the pattern is that the center of the antenna pattern is slightly bigger or smaller than it would be without the correction.

The FOV measurements were made in three consecutive scan averages of 60 minutes each. Each scan had a linear angular-scan portion, a view of the ambient target, and a view of the center of the pattern. The linear portion of the scans covered nominal scan angles of 359.94°–358.85°, 358.90°–357.869°, and 359.84°–0.905°, respectively. The ambient and center view showed that the source and instrument were stable over the measurement time. The three scans were "stitched" together by determining the average difference of two scans in the overlapping region. This difference was subtracted from the outlying scan. The overlapping region was averaged with a weight that changed linearly from 0 to 1 over the overlap region so that there were no discontinuities in the data. The maximum point in the scan was then shifted to zero and a complex Fourier transform was taken with no apodization. After dividing out the effects of the slit and the sample integration, the corrections described earlier in this section were applied, and the correlation function was set to zero beyond ± one diameter of the primary. The magnitude of the correlation functions are shown in Fig. 2.

These autocorrelation functions are then back Fourier transformed and the imaginary part of the result is discarded. The resulting FOV patterns are shown in Fig. 3. The absolute value of the pattern amplitude has been taken to avoid taking the logarithm of a negative number. Note that the sidelobes are much larger for the V bands than the H bands and that there are also small differences in the width and position. Nonetheless, the patterns for bands within the same mixer are similar as expected when there is no significant frequency dependence in the patterns. The patterns used in the forward model [5] for the MLS geophysical data retrievals [6] for bands 15–17 are the average

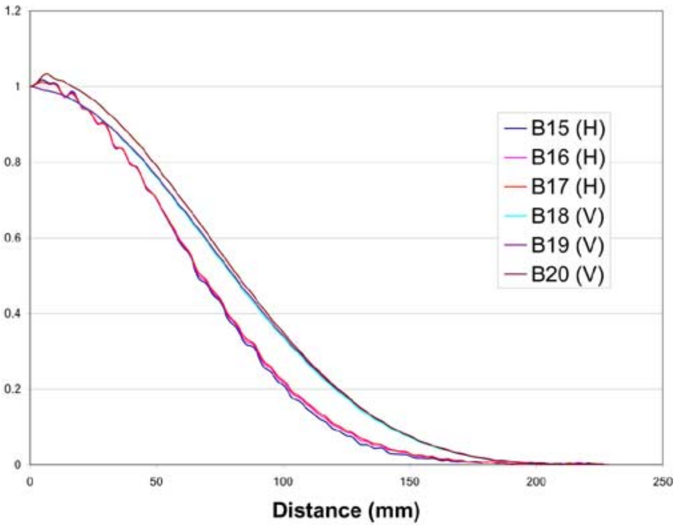

Fig. 2. FOV aperture autocorrelation function. The legend refers to band designations given in Table I.

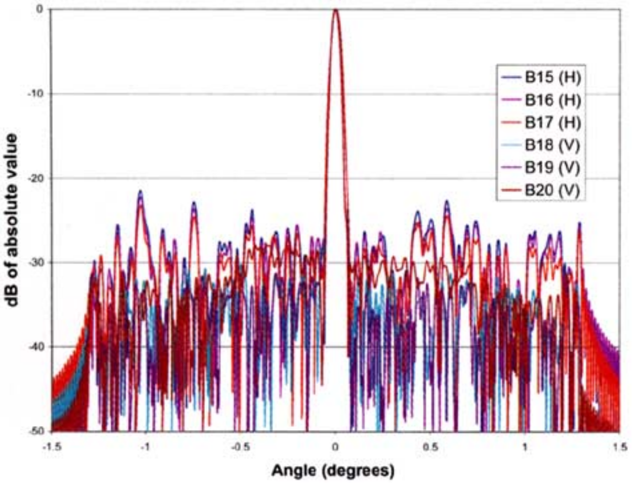

Fig. 3. FOV one-dimensional pointing response. The legend refers to band designations given in Table I. The estimated noise level is −34 dB and the uncertainty in the offset is −24 dB.

TABLE II
THz Vacuum FOV Results

Band(pol.)	Center(°)	FWHM (°)	Beam Eff.
15 (H)	-0.7277±0.0007	0.0463±0.0023	1.014±0.020
16 (H)	-0.7279±0.0007	0.0452±0.0023	1.011±0.020
17 (H)	-0.7283±0.0007	0.0448±0.0023	1.012±0.020
18 (V)	-0.7292±0.0007	0.0387±0.0023	0.996±0.020
19 (V)	-0.7301±0.0007	0.0384±0.0023	0.996±0.020
20 (V)	-0.7306±0.0007	0.0387±0.0023	1.027±0.020

of the patterns shown here for these bands, while the pattern used for bands 18–20 are the average of patterns for bands 18 and 19. The center of these patterns was fitted with a Gaussian down to −5 dB. The results of the fit for center, full-width at half-maximum (FWHM), and beam efficiency are shown in Table II, along with 1σ uncertainties. The center position has an arbitrary offset due to alignment of the calibration test parabola with respect to the instrument, but the differences between the bands are significant. The beam efficiency is the fraction of the total pattern area that is within ±2.5× FHWM within the vertical direction. The beam efficiency can be greater than unity due to effects of noise.

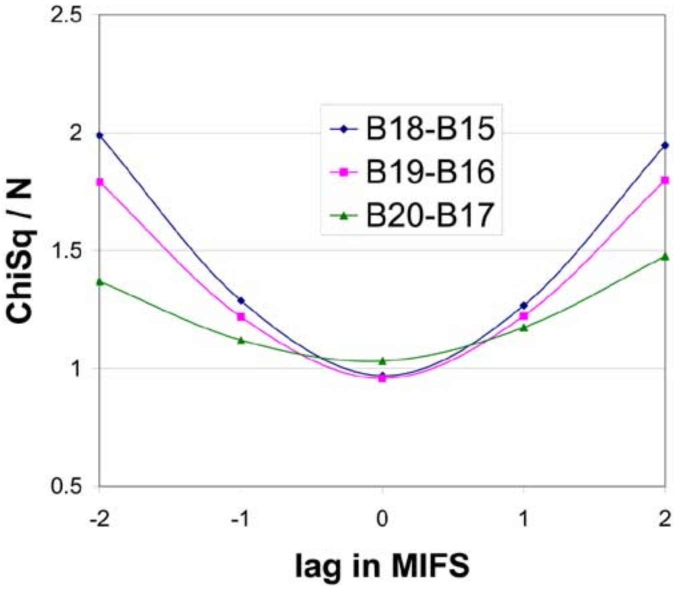

Fig. 4. V-H pointing offset. The legend refers to band designations given in Table I.

In vacuum, it is not practical to determine the THz boresight with respect the spacecraft mount points. To determine absolute boresight, the spacecraft mount points were located relative to the axis defined by the primary focal aperture using theodolite measurements. Measurements in air of the boresight showed that the visible center of the focal aperture was located at a scan angle of −1.050° ± 0.010°, while the THz centers were located at −1.0679° ± 0.0002° and −1.0671° ± 0.0006° for the H and V mixers, respectively. The THz measurements of the centers were determined by fitting the uncorrected patterns to a Gaussian down to −5 dB. For reference, the angular diameter of the focal aperture is 0.15°. Offsets from the vacuum measurements are due to distortion of the measurement equipment under vacuum and are not significant to the calibration.

B. Postlaunch Boresight Calibration

After launch, relative boresight positions of the two mixers were obtained by making a constant-velocity scan of the atmosphere for 8 h on August 11, 2004. After radiometric calibration, compute

$$\chi^2_\ell = \sum_{i,k} \frac{[R(V)_{i,k} - R(H)_{i,k+\ell}]^2}{\sigma(V)^2_{i,k} + \sigma(H)^2_{i,k+\ell}} \qquad (1)$$

where $R(V)_{i,k}$ and $R(H)_{i,k}$ are the radiances in channel i and MIF k for the V and H mixers, respectively. $\sigma(V)_{i,k}$ and $\sigma(H)_{i,k}$ are the estimated precisions for the corresponding radiances. χ^2_ℓ is shown for the three independent pairs of bands in Fig. 4. The vertical velocity of the boresight on the limb was 823 m/MIF. The positions of the minima are 13.5, −2.6, and −94.9 m for the three bands, and are negligible compared with uncertainties.

Calibration of pointing offsets between the GHz and THz module can be tested using the moon when it enters the MLS FOV once every 14 days. Preliminary analysis of the available opportunities indicate that the offsets have not changed from their prelaunch values [4].

IV. SPECTRAL CALIBRATION

The requirements for the THz spectral calibration are essentially the same as those for the GHz channels described in [8]. Because of water vapor attenuation, all THz measurements must be made in vacuum. The approach for both side-band and spectral response calibrations is to use a high-resolution Fabry–Perot resonator that is illuminated by the parabola-fed medium pressure mercury arc source used for the FOV calibration. The slit in the source cavity is replaced with a 1.6-mm circular aperture matching the instrument focal aperture. The mercury arc provides a stable continuum source with an equivalent brightness of 1000–1200 K and can be operated in vacuum. A solenoid-actuated shutter is located near the Mercury arc source to allow differencing of signals with the source on and the source blocked. The Fabry–Perot resonator is the same unit that has been use for many years in our FILOS balloon experiment for measuring OH [7]. The distance between resonances [free spectral range (FSR)] is 1.5 GHz and the width of the resonance is 50 MHz. The resonator can scan 140 μm and is vacuum compatible. The filterbank response is observed as a function of Fabry–Perot length and can provide both side-band response and spectral response down to a resolution of 50 MHz. Since no appropriate spectrally narrow swept sources exist in the THZ region, RF sweeps of the IFs are used for the narrow-band (<20 MHz) characterization of the spectral response.

The Fabry–Perot filter is step-scanned with a 4-s observation interval with the shutter open and a 4-s interval with the shutter closed per step for a total of 385 steps. The time for a sweep is 80 min after allowance is made for dead time. The FILOS Fabry–Perot has 40% throughput at resonance. Combined with the expected brightness of the source, the predicted contrast at resonance is (1200–300 K) $\times$ 0.4 $=$ 360 K. For the 6-MHz filterbank channels, $\Delta T_{\mathrm{rms}} = 3.0$ K for 4 s, or 1.2% after allowance for differencing. For the 96-MHz filterbank channels, the signal averaged over the filter is 230 K, while $\Delta T_{\mathrm{rms}} = 0.76$ K, for 0.45% precision under the same conditions. (Actual performance is degraded because of standing wave interactions between the LLO and the Fabry–Perot.) Radiometric offset comes from the shutter differencing, while radiometric gain comes from assuming that the source output and Fabry–Perot throughput are both independent of frequency. Fabry–Perot length calibration comes automatically from measuring the repeat length for the scan (equal to half the wavelength). We took measurements for four scans for a total measurement time of 320 min.

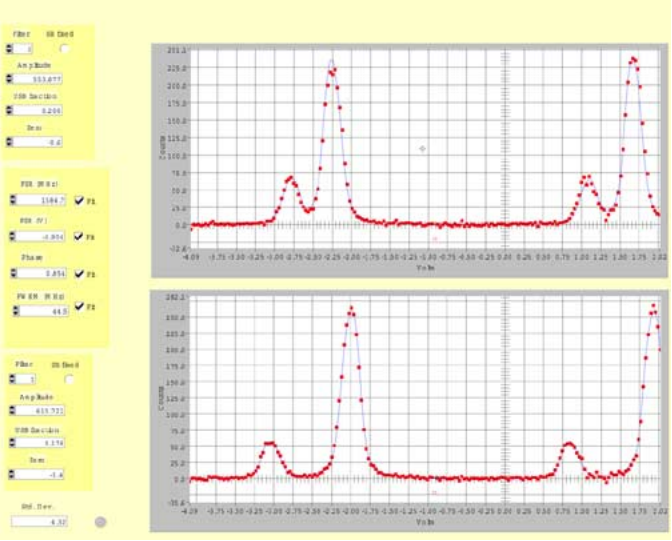

Fig. 5. Fitting side-band response.

TABLE III
TERAHERTZ SIDE-BAND RESULTS

Band	LSB fraction	slope * GHz
15	0.9605±0.0010	-0.0053±0.0038
18	0.9481±0.0017	-0.0027±0.0066
16	0.8308±0.0019	-0.0463±0.0067
19	0.8123±0.0032	-0.0473±0.0113
17	0.3896±0.0031	-0.0620±0.0123
20	0.3831±0.0016	-0.0619±0.0064

Analysis is simple in principle but somewhat more complicated in practice. The response from each channel is essentially the integral of the Fabry–Perot response multiplied by the filter response:

$$R(V)_i = Z_i + \sum_{k=0}^{1} \int \frac{A_{i,k} F(\nu)_{i,k} d\nu}{1 + |Q \sin\theta(\nu)|^2} \tag{2}$$

with

$$\theta(\nu) = \pi\nu(1 + V/\mathrm{FSR}_L)/\mathrm{FSR}_f + \pi\phi \tag{3}$$

where V is the etalon tuning voltage, $A_{i,k}$ is an amplitude for channel i and side-band k, Z_i is a offset, $F(\nu)_{i,k}$ is the known filter response, Q is related to the width of the Fabry–Perot resonance, FSR_L is the free spectral range in voltage units, FSR_f is the free spectral range in frequency units, and ϕ is a phase shift. The values of Q, FSR_L, and FSR_f are fit for all scans and all bands. The values of ϕ, Z_i, and $A_{i,k}$ are fit for each scan and each band. The quantity of interest is the lower side-band fraction: $A_{i,0}/(A_{i,0} + A_{i,1})$.

We fit the side-band ratio with a graphic interface that allows user intervention before starting the least square fit for a given scan and band. An example of a fit is shown in Fig. 5 for channel 0 and 1 in band 16. The horizontal axis is the voltage used to tune the length over 80 μm.

Note that, for a few channels, the upper and lower side-band resonances occur at the same etalon length. For such channels the side-band fraction cannot be determined without scanning several wavelengths. We found it expedient to fit the resulting side-band fractions that were determinable to a straight line versus the average second IF frequency of the filter (less 900 MHz).

Final side-band calibration was performed after installation of the quartz quarter wave plate. The midband side-band fraction and its slope are given in Table III. A graphical depiction of the side-band results (before the straight line fit) are shown

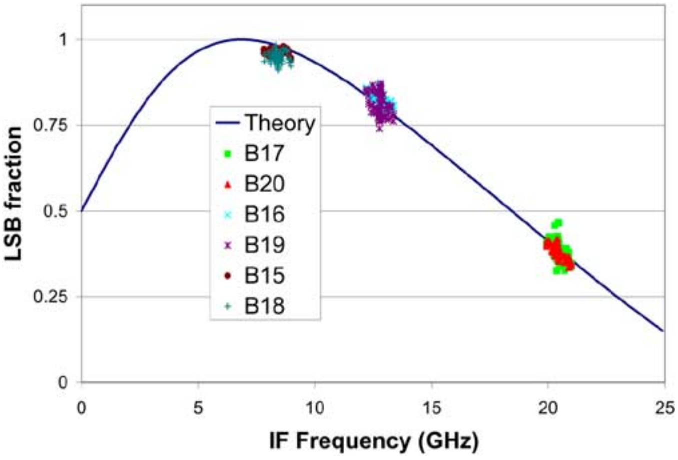

Fig. 6. Lower side-band fraction compared with diplexer model.

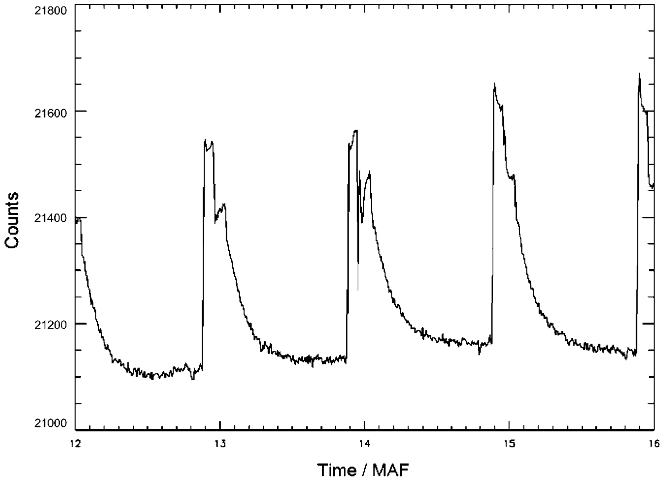

Fig. 7. Typical raw filterbank counts for orbit 1 on Day 243 in 2004 (band 18, channel 1).

in Fig. 6. The expected side-band performance for the diplexer is shown as the solid line, where the diplexer free spectral range and frequency offset are adjusted to 36.57 and 6.52 GHz, respectively. Note that the side-band fraction and slope for each band are consistent with a model in which all the side-band performance is explained by the diplexer throughput.

V. RADIOMETRIC CALIBRATION

The THz radiometer calibration is similar in many respects to the MLS GHz radiometers. However, the THz Laser Local Oscillator presents special problems that influence the design of the calibration algorithm because the GLLO power varies significantly with time. Fortunately, the mixer is driven by a constant-current source and the mixer voltage is a measure of the GLLO power. The mixer bias voltage is recorded every MIF and can be used to correct the raw radiometer counts for variations in GLLO power. In practice, increases in GLLO power cause increases in in IF power that can look like changes in radiance. Over small variations in GLLO power, IF power can be presumed to be a linear function of the mixer bias voltage.

The radiometric calibration is obtained from an on-board ambient-temperature black body and a space view located at a scan angle of 3.2° above the nominal boresight. The on-board black body is a grooved cylindrical-shaped target located behind the scan mirror 180° away from the boresight. The grooves in this target have a 60° included angle so that there are at least 3 reflections in the grooves. The target is coated with white Hincom paint that has a measured 4% reflectivity at 119 μm. Therefore, the theoretical effective emissivity is better than 99.99%. The temperature of this target is determined by four platinum resistance thermometers embedded in the back side of the target. The front surface of the target is shadowed by the scan mirror 96% of the time. During the time that the target is exposed, the solid angle represented the limb-view aperture is less than $0.025 \times 2\pi$ Sr so that the temperature of the surface of the target is not unduly influenced by radiative effects. Even with no thermal conduction within the paint, the temperature of the surface would only be 0.3 K lower than the body of the target.

The effects of nonlinearity for the GHz radiometers are covered in [8], where it is shown that nonlinearities are small. The THz and GHz modules share the same design of IF down conversion and filterbank. Here the change in IF power is smaller in relation to the total IF power than in any of the GHz radiometers, and the nonlinearities should be correspondingly smaller.

Fig. 7 shows typical filterbank counts for four successive MAFs. The limb scan portion of each MAF includes MAF fraction 0.0–0.8 (0–19.1 s). The space view follows 0.4 s later, and the target view follows after that. The space view has the lowest counts and the target view has the largest counts.

A. *GLLO Nominal Operation*

In normal operation, the instrument computer requests telemetry data (including mixer bias voltage) each MIF. The far-infrared laser in the GLLO operates in open-loop mode until a request is made to perform a reoptimization (typically in MIF 139). This command is sent before the telemetry request command. If the laser needs reoptimization, or if a specified number of MAFs have elapsed, the laser is reoptimized.

B. *Mixer Bias Handling*

Since the mixer bias voltage will be used for correcting the radiometric counts, it is important to check that the values are valid. Since the maximum bias voltage is less than 2.5 V, the value of 2.5 V is used to indicate an error. If the GLLO is executing a reoptimization, it will respond to a telemetry request with a negative acknowledge (NAK) message. If this is the case, the ground software sets the bias to 2.5 V. The bias voltage is 0.85 V for no GLLO power and decreases as GLLO power increases. Therefore, a threshold voltage of intermediate value, typically 0.61 V, can discriminate between good GLLO operation and other states that can include inadequate GLLO drive, invalid mixer bias, and a GLLO reoptimization event. For simplicity, any state that produces voltage below threshold will be designated as valid mixer bias.

C. *Correction for GLLO Power and Radiometric Gain*

The first step for THz calibration is to take one orbit of normal radiometric data (240 MAFs or 98 min) and determine boundaries where either the laser has relocked or where there is a gap in the data. Then perform a 2-parameter fit for GLLO sensitivity and radiometric gain to the subset of the calibration data that have valid mixer bias

$$C_{i,k} = C^0_{i,k} + d_{\mathrm{LLO},i}(B_k - \hat{B}_k) + d_{\mathrm{CAL},i}(\mathrm{TE}_k - \hat{\mathrm{TE}}_k) \tag{4}$$

where $C_{i,k}$ is the calibration count for channel i and time sample k, B_k is the mixer bias and $\hat{B}_k$ is the average mixer bias within the boundary that contains time sample k. TE_k is the calibration radiometric scene temperature and $\hat{\mathrm{TE}}_k$ is the average value of TE_k within the boundary. We are assuming that the gain, $d_{\mathrm{CAL},i}$, is not influenced significantly by GLLO power, because the change in IF power due to changes in scene radiance is 1% of the total. The radiometric temperature is the black-body radiance in temperature units, i.e., at the GLLO frequency

$$\mathrm{TE}_k = \frac{121.1\ \mathrm{K}}{\exp(121.1\ \mathrm{K}/T_k) - 1} \tag{5}$$

where $h\nu/k = 121.1$ K. Note that T_k takes on the temperature of the calibration target when looking at the target and takes on the cosmic background temperature when looking at space. With no appreciable loss in accuracy, assume that TE at the signal upper and lower side-bands is the same as the value at the GLLO frequency. Note that d_{LLO} and d_{CAL} can be determined without fitting for C^0 since the correlation with C^0 is identically zero. Also note that the least-squares matrix is independent of i, and much of the least-squares solution is common to all channels. The validity of the fit depends on assuming that temporal drifts in the counts are uncorrelated with GLLO bias or the temperatures of the calibration scenes. The use of local averages allows for discontinuities in counts when the GLLO is relocked.

The partially calibrated counts are then

$$\mathrm{TS}_{i,k} = \frac{C_{i,k} - d_{\mathrm{LLO},i}(B_k - \hat{B})}{d_{\mathrm{CAL},i}} \tag{6}$$

where $\hat{B}$ is the data set average of mixer bias. The correction of counts to temperature units should be applied to the whole data set, not just the calibration data subset. The GLLO correction is only applied to data with a valid mixer bias. TS still contains a substantial offset which is of the order of T_{sys}. In fact, if $C_{i,k}$ is corrected for the offset counts, then TS is equal to the y-factor T_{sys} plus the scene temperature. Fig. 8 shows typical values of TS for the same data given in Fig. 7.

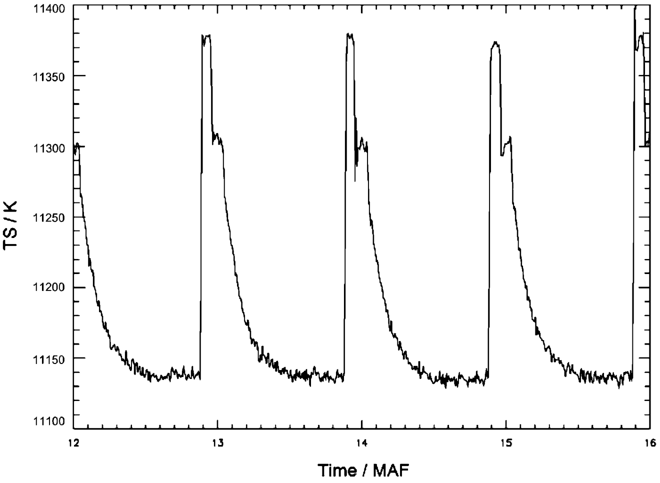

Fig. 8. Typical partially calibrated radiance for Orbit 1 on Day 243 in 2004 (band 18, channel 1).

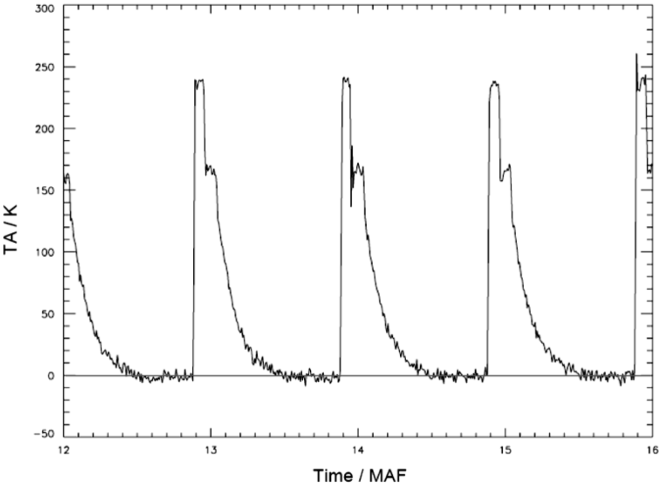

Fig. 9. Typical calibrated radiance for Orbit 1 on Day 243 in 2004 (band 18, channel 1).

D. Correction for Offset

The second step is to subtract offsets so that the calibrations are equal to their respective radiative temperatures. Like the GHz calibration, this subtraction will involve piece-wise quadratic interpolation of the fitted calibrations. Even after correction for GLLO power variation, the radiometer response, TS, shows discontinuities in slope at times where there is a GLLO reoptimization. Accordingly, the piece-wise fitting will use continuous segments of data with valid mixer bias. For a given MAF, calibration data is chosen in a window centered in the MAF at time t_c with a width w such that $|t_k - t_c| < w$ and fit

$$\mathrm{TS}_{i,k} = \mathrm{TE}_k + a_i + b_i(t_k - t_c) + c_i(t_k - t_c)^2 \tag{7}$$

where k is limited only to calibrations within the window and within the segment with valid mixer bias. If the range of data included in the fit spans only the time interval of one MAF, fit only for a_i. If it spans a time interval of 2 MAFs, then fit for a_i and b_i, otherwise perform the full quadratic fit. Typically, $w = 2$ MAF, although larger values should be possible if the system stability justifies it. Again, the least-squares matrix is independent of i so computation speed can be improved by inverting the matrix only once. Then

$$\mathrm{TA}_{i,k} = \mathrm{TS}_{i,k} - a_i - b_i(t_k - t_c) - c_i(t_k - t_c)^2 \tag{8}$$

is applied to all data within the MAF.

Fig. 9 shows typical values of TA for the same data given in Figs. 7 and 8.

VI. PERFORMANCE

Fig. 10 shows typical in-orbit y-factor T_{sys}, defined above as $(\mathrm{TS}_i - \mathrm{TA}_i)$, for Bands 15–20. The horizontal axis is equal to $([\mathrm{band} - 15] \times 25 + \mathrm{filterbank\ channel} - 1)$. This measure of system performance represents a lower limit on radiometric noise through the well-known radiometer equation [9]

$$\sigma(\mathrm{TA})_i \geq \mathrm{TS}_i/\sqrt{B\tau} \tag{9}$$

where $\sigma(\mathrm{TA})_i$ is the noise, B is the noise bandwith, and τ is the integration time. Bands 17 and 20 have larger system temperature and noise because these bands are located at a high IF centered at 20.5 GHz. This poorer noise performance was anticipated, and the system requirements are a factor of 3 less stringent in these bands.

The actual noise performance is estimated by computing the variance of the calibration views from their expected values

$$\sigma(\mathrm{TA})_i = \sqrt{\frac{1}{N}\sum_k (\mathrm{TA}_{i,k} - \mathrm{TE}_{i,k})^2} \tag{10}$$

where the sum is over all calibration views and N is the number of such views. Fig. 11 shows typical values of $\sigma(\mathrm{TA})_i$ using the same horizontal axis as Fig. 10. The larger noise at the center of each band is due to the narrower bandwidth of the filters, which go from 6 MHz at band center to 96 MHz at band edge. The larger value at channel 21 of band 15 (the left X in Fig. 11) is due to leakage from the Aura high data-rate transmitter at 8.16 GHz, whose frequency falls within the IF passband of Bands 15 and 18. The other potential interference at channel 21 of band 18 (the right X in Fig. 11) also appears on occasion. This interference was known to be a potential problem prior to launch. The levels are low enough so they are not apparent in the y-factor T_{sys} shown in Fig. 10. Nonetheless, these two channels are not used in the retrievals.

The ratio of estimated precision to the expectation from y-factor T_{sys} is unity (within the noise level) at the band centers. At the band edge, the ratio can grow to as large as 2.5 due to gain fluctuations. These gain fluctuation are usually considerably smaller in the GHz bands. We suspect that the explanation for the larger THz ratio is related to GLLO power fluctuations that are not completely corrected for by the MLS THz radiometric calibration with linear mixer-voltage compensation.

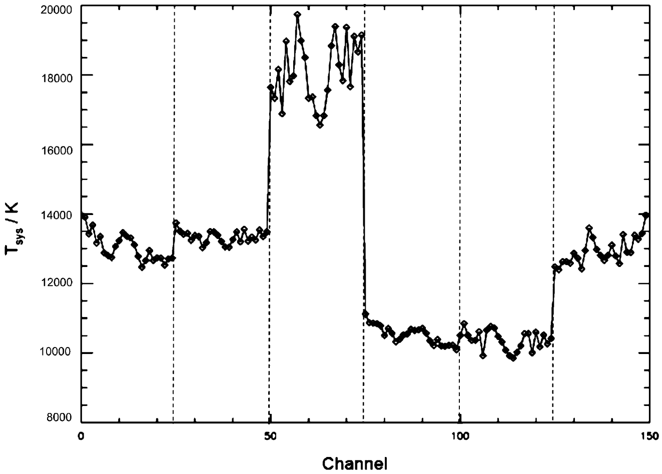

Fig. 10. Typical y-factor T_{sys} for Orbit 1 on Day 225 in 2004.

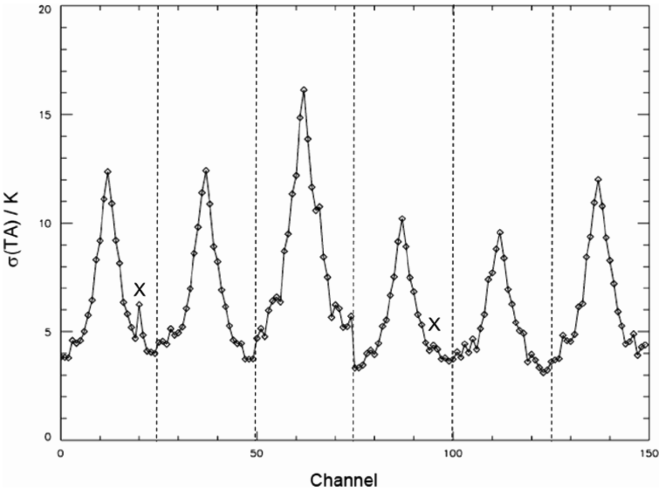

Fig. 11. Typical radiometric precision for Orbit 1 on Day 225 in 2004. X indicates location of potential Aura transmitter interferrence.

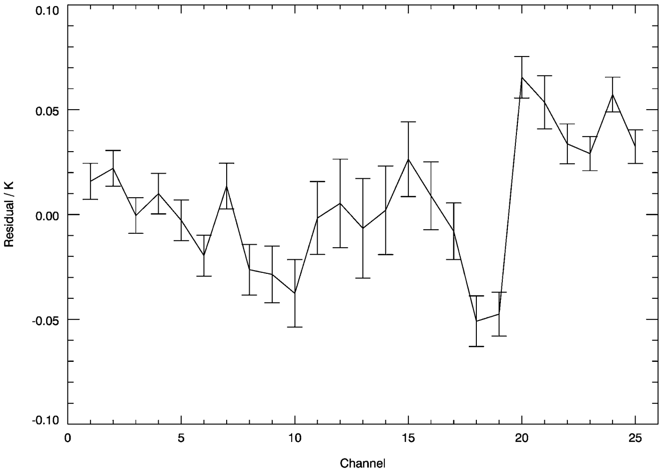

Fig. 12. Radiometric residual with equivalent integration time of 151 min. Error bars are the estimated precision in the residual.

Additional test of radiometric calibration and FOV understanding was obtained by a scan sequence that positioned the scan mirror for 10 s at an angle of 10° above the Earth followed by 10 s at an angle of 12°, followed by a 1-s view of the calibration target. The scan was repeated for a total of 12 h. The expectation is that the calibrated radiance should be zero except for a small ($<$1%) contribution from scattering of the Earth radiance into the instrument at angles $>$10°. A residual was obtained by averaging the calibrated radiance for the 12-h data set for each angle and then taking the difference of the data for the two angles. This difference showed a 1-K baseline offset consistent with expectations. After the average offset was removed for each polarization, as is done in level 2 software, the remaining spectrally varying component was averaged for the four OH bands. Fig. 12 shows the residual signal for an equivalent integration of 151 min. The error bars are the estimate precision for the average shown. For

TABLE IV
CONTRIBUTION TO UNCERTAINTY

type	contribution
precision	12.5 K
boresight	10.1 K
FWHM	0.053 K
beam eff.	2.0 %
spectral	0.1 %

reference, a 3-km-wide layer of OH at 20 km with typical 1 ppt concentration yields a radiance temperature of 0.61 K at a 20-km tangent height, more than 10× larger than the residuals.

VII. CONCLUSION

The MLS THz module alignment and calibration uses techniques adapted from both longer and shorter wavelengths. The optics were made with surfaces that were reflecting in the visible so that alignment could be achieved with white-light tools such as theodolites and autocollimators. The use of a Gregorian telescope facilitated referencing the visible light properties of the optics to the THz beam. Both the FOV calibration and spectral calibration exploited a mercury arc source originally developed for far-infrared spectroscopy. On the other hand, radiometric calibration is based on microwave techniques.

Table IV shows derived uncertainties for different parts of the calibration. The uncertainties have been converted in some cases by using the radiance versus scan angle for typical daytime conditions. The precision is for 1 MIF integration in the center of band 15. The boresight uncertainty in Table IV is equal to the value from Table II multiplied by the largest derivative of radiance with respect to scan angle. The radiance retrieval [6] corrects for the boresight offset, so the boresight offset does not directly contribute to the uncertainty of the retrieved OH. The FWHM uncertainty in Table IV is equal to the value from Table II multiplied by the largest second derivative of radiance with respect to scan angle. Uncertainties in the beam efficiency and spectral calibration of the side-band fraction are shown in percent because these contributors multiply the radiance and ultimately the retrieved OH.

The contributions of calibration errors to the final OH retrievals are very small. For averages of large numbers of profiles, e.g., monthly zonal means, the uncertainty at some altitudes will be dominated by the beam efficiency uncertainty of 2%.

ACKNOWLEDGMENT

The author would like to thank the many scientists and engineers in the MLS project at the Jet Propulsion Laboratory, Pasadena, CA, who contributed to the design and calibration for the THz module.

REFERENCES

[1] G. A. Blake, J. Farhoomand, and H. M. Pickett, "The far-infrared rotational spectrum od $X^2\Pi$ OH," *J. Mol. Spectrosc.*, vol. 115, pp. 226–228, 1986.

[2] M. C. Gaidis, H. M. Pickett, C. D. Smith, S. C. Martin, R. P. Smith, and P. H. Siegel, "A 2.5-THz receiver front end for spaceborne applications," *IEEE Trans. Microw. Theory Tech.*, vol. 48, no. 4, pp. 733–739, Apr. 2000.

[3] J. W. Waters, L. Froidevaux, R.S. Harwood, R. F. Jarnot, H. M. Pickett, W.G. Read, P. H. Siegel, R. E. Cofield, M. J. Filipiak, D. A. Flower, J. R. Holden, G. K. Lau, N. J. Livesey, G. L. Manney, H. C. Pumphrey, M. L. Santee, D. L. Wu, D. T. Cuddy, R. R. Lay, M. S. Loo, V. S. Perun, M. J. Schwartz, P. C. Stek, R. P. Thurstans, M. A. Boyles, K. M. Chandra, M. C. Chavez, G.-S. Chen, B. V. Chudasama, R. Dodge, R. A. Fuller, M. A. Girard, J. H. Jiang, Y. Jiang, B. W. Knosp, R. C. LaBelle, J. C. Lam, K. A. Lee, D. Miller, J. E. Oswald, N. C. Patel, D. M. Pukala, O. Quintero, D. M. Scaff, W. Van Snyder, M. C. Tope, P. A. Wagner, and M. J. Walch, "The Earth Observing System Microwave Limb Sounder (EOS MLS) on the Aura Satellite," *IEEE Trans. Geosci. Remote Sens.*, vol. 44, no. 5, pp. 1066–1074, May 2006.

[4] R. E. Cofield and P. C. Stek, "Design and field-of-view calibration of 114–660-GHz optics of the Earth Observing System Microwave Limb Sounder," *IEEE Trans. Geosci. Remote Sens.*, vol. 44, no. 5, pp. 1166–1181, May 2006.

[5] W. G. Read, Z. Shippony, M. J. Schwartz, N. J. Livesey, and W. Van Snyder, "The clear-sky unpolarized forward model for the EOS Microwave Limb Sounder (MLS)," *IEEE Trans. Geosci. Remote Sens.*, vol. 44, no. 5, pp. 1367–1379, May 2006.

[6] N. J. Livesey, W. V. Snyder, W. G. Read, and P. A. Wagner, "Retrieval algorithms for the EOS Microwave Limb Sounder (MLS)," *IEEE Trans. Geosci. Remote Sens.*, vol. 44, no. 5, pp. 1144–1155, May 2006.

[7] H. M. Pickett and D. B. Peterson, "Stratospheric OH measurements with a far-infrared limb observing spectrometer," *J. Geophys. Res.*, vol. 98, pp. 20 507–20 515, Nov. 1993.

[8] R. F. Jarnot, V. S. Perun, and M. J. Schwartz, "Radiometric and spectral performance and calibration of the GHz bands of EOS MLS," *IEEE Trans. Geosci. Remote Sens.*, vol. 44, no. 5, pp. 1131–1143, May 2006.

[9] J. D. Krauss, *Radio Astronomy*. New York: McGraw-Hill, 1966.

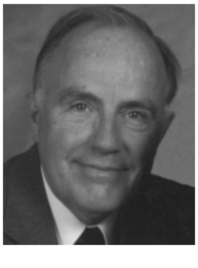

Herbert M. Pickett (M'83) received the B.A. degree from Williams College, Williamstown, MA, in 1965 and the Ph.D. degree in physical chemistry from the University of California, Berkeley, in 1970.

From 1970 to 1973, he was a Postdoctoral Fellow at Harvard University, with E. Bright Wilson, Jr. In 1973, he was a Miller Fellow at the University of California, Berkeley. From 1973 to 1978, he was an Assistant Professor at the University of Texas, Austin. Currently, he is a Senior Research Scientist and a Co-Investigator for the Aura Microwave Limb Sounder, Jet Propulsion Laboratory, California Institute of Technology, Pasadena.